Stony Brook University

Shock Waves in a 2D Riemann Problem Having Pure Rarefaction Data

A Dissertation Presented

by

Xiaomei Ji

to

The Graduate School in Partial Fulfillment of the Requirements for the

Degree of

Doctor of Philosophy

in

Applied Mathematics and Statistics

Stony Brook University

August 2009

Stony Brook University

The Graduate School

Xiaomei Ji

We, the dissertation committee for the above candidate for the Doctor of Philosophy degree, hereby recommend acceptance of this dissertation.

James Glimm
Dissertation Advisor
Professor and chair of Department of Applied Mathematics and Statistics

Xiaolin Li
Chairperson of Defense
Professor of Applied Mathematics

Xiangmin Jiao
Assistant Professor of Applied Mathematics

David Ebin
Professor and chair of Department of Mathematics
Outside Member

This dissertation is accepted by the Graduate School.

Lawrence Martin
Dean of the Graduate School

Abstract of the Dissertation

Shock Waves in a 2D Riemann Problem Having Pure Rarefaction Data

by

Xiaomei Ji

Doctor of Philosophy

in

Applied Mathematics and Statistics

Stony Brook University

2009

It is perhaps surprising for a shock wave to exist in the solution of a rarefaction Riemann problem for the compressible Euler equations in two space dimensions. We present numerical evidence and generalized characteristic analysis to establish the existence of a shock wave in such a 2D Riemann problem, defined by the interaction of four rarefaction waves. We consider both the customary configuration of waves at right angles and also an oblique configuration for the rarefaction waves. Two distinct mechanisms for the formation of a shock wave are discovered as the angle between the waves is varied.

Table of Contents

List of Figures

List of Tables

Acknowledgements

I very much thank my advisor, Professor James Glimm, for the very important and interesting topics in conservation laws and very helpful discussions under his direction and his continuous support. Professor Glimm is very distinguished in many research areas, and I have learned a lot from him. I also thank all my collaborators and those who helped me in academic career. I hope this thesis will be dedicated to Professor Glimm on his 75 birthday.

I would like to dedicate this thesis to my father and my beloved mother. My mother suffered greatly and passed away in 1997, but she loved me very much and she tried best to support me. She never delayed my study at any time even if when she needed me most. She taught me how to become an honest, decent and upright person since I was a little child. She was very smart and she was an excellent physician. She also told me how to try to overcome difficulty. I missed her very much.

Chapter 1

Introduction

1.1 Historical review

In 1860, B. Riemann [8, 27] put forward and studied the initial-value problem with the simplest discontinuous initial data for isentropic Euler equations in gas dynamics:

$$\begin{aligned} &\tfrac{\partial \rho}{\partial t} + \tfrac{\partial (\rho u)}{\partial x} = 0, \\ &\tfrac{\partial (\rho u)}{\partial t} + \tfrac{\partial (\rho u^2 + p)}{\partial x} = 0, \\ &(\rho, u) = \begin{cases} (\rho_1, u_1), & x > 0, \\ (\rho_2, u_2). & x < 0, \end{cases} \end{aligned} \tag{1.1.1}$$

where ρ, p and u are the density, pressure and velocity, respectively, $p = A\rho^\gamma$, where $A > 0$ is constant and $\gamma > 1$ is the adiabatic index. The initial data are given by two arbitrary constant states. It is natural to construct self-similar solutions, on the basis of the fact that both the equations and the initial data are self-similar. Riemann's solutions uncover the elementary waves of isentropic flow: shock waves and rarefaction

waves. This result was extended to adiabatic flow by Courant and Friedrichs in the 1940s, and a new kind of elementary waves, slip lines, was identified. The initial data of a general Riemann problem is constant along radial directions from an origin and it is piecewise constant as a function of angle. In 1957, P. Lax [19] published the theory of small solutions to the Riemann problem for 1D strictly hyperbolic system of conservation laws. Lax's theorem not only proves the existence of solutions, but also describes the structure of the solution. Moreover, Lax expounded many fundamental concepts: genuine nonlinearity, entropy condition, shock waves, etc. After these developments, 1D Riemann problems for hyperbolic system of conservation laws have given rise to many interesting results.

In 1965, J. Glimm [12] contributed a well-known existence theory. Consider the quasilinear system of equations, where v, f are vector-valued functions.

$$v(x,t)_t + f(v(x,t))_x = 0, \quad -\infty < x < +\infty, t \geq 0. \tag{1.1.2}$$

Let the distance between the initial data $v(\cdot, 0)$ and a constant $\tilde{v}$ be defined either

$$d_0 = \|v(\cdot,0)) - \tilde{v}\|_\infty (1 + \mathrm{Var}(v(\cdot,0))), \tag{1.1.3}$$

or

$$d_1 = \|v(\cdot,0)) - \tilde{v}\|_\infty \mathrm{Var}(v(\cdot,0)), \tag{1.1.4}$$

where Var(u) denotes the total variation of the function of u. That v is a weak solution with initial data $v(x,0)$ means that v is a bounded measurable function and

that

$$\int_0^{+\infty}\int_{-\infty}^{+\infty}(\phi_t v+\phi_x f(v))dxdt+\int_{-\infty}^{+\infty}\phi(x,0)v(x,0)dx=0. \tag{1.1.5}$$

for all smooth function ϕ which are identically zero outside some bounded set.

Theorem 1.1 Let the equations (1.1.2) be hyperbolic, strictly nonlinear and smooth in a neighborhood of $\tilde{v}$. There is a $K<\infty$ and a $\delta>0$ with the following property. If the initial data $v(x,0)$ are given so that $d_1\leq\delta$, then there is a weak solution $v(x,t)$ of (1.1.2) defined for all x and all $t\geq 0$ with initial data $v(x,0)$ such that

$$\|v-\tilde{v}\|_\infty\leq K\|v(\cdot,0)-\tilde{v}\|_\infty, \tag{1.1.6}$$

$$\mathrm{Var}(v(\cdot,t))\leq K\mathrm{Var}(v(\cdot,0)),\quad t\geq 0, \tag{1.1.7}$$

$$\int_\infty^\infty |v(x,t_1)-v(x,t_2)|\ \ dx\leq K|t_1-t_2|\mathrm{Var}(v(\cdot,0)). \tag{1.1.8}$$

If there is a coordinate system $w_1,...w_N$ defined in a neighborhood of $\tilde{v}$ which consists of Riemann invariants (for example $N=2$), and if the initial data $v(x,0)$ are given so that $d_0\leq\delta$,then there is a weak $v(x,t)$ of (1.1.2) defined for all x and all $t\geq 0$ with initial data $v(x,0)$ such that (1.1.6) and (1.1.7) hold.

The proof of Theorem 1.1 implements Glimm scheme (depends upon a random choice) and solutions of Riemann problem through Theorem 4.1. It solves the existence of solutions under small initial data in 1D system of conservation laws. It is one of the most important contributions in conservation laws.

In 1990, Zhang and Zheng [31] analyzed 2D Riemann problems for compressible Euler equations. They structured boundaries of the interaction of four planar waves coming from infinity with various cases. Each boundary is composed of characteris-

tics, shocks and sonic curves. Based on the analysis of 1D interaction of waves and of 2D Riemann problems of scalar conservation laws and reflection of shocks, they established a set of conjectures for the wave patterns in the domains of interaction.

In 1959, Gelfand [11] stated "the Riemann problem plays a special role in the theory of quasilinear hyperbolic systems. As we will show, the Riemann problem are important in the study of existence, uniqueness and asymptotic behavior of solutions as $t \to \infty$ for the corresponding Cauchy problem. Besides, the study of the Riemann problem has its own sake." It is widely recognized that the Riemann problem plays a key role of as a building block for theory, numerical simulations and applications in the entire conservation laws fields.

1.2 Related work on shock reflections

Shock reflection in gas dynamics has long been an open problem. When a plane shock hits a wedge, it experiences a reflection-diffraction process, and then a self-similar reflected shock moves outward as the original shock moves forward in time. The complexity of reflection-diffraction configurations was first reported by Ernst Mach [26] in 1878, and experimental, computational, and asymptotic analysis has shown that various patterns of shock reflection-diffraction configurations may occur, including regular reflection and Mach reflection. Two-dimensional Riemann problems have been proposed for the compressible Euler equations as a general approach to the shock reflection problem [31]. Numerical simulations for this type of data have been performed by Chang, Chen and Yang [2], Schulz-Rinne, Collins and Glaz [28], Lax and Liu [20],[25], Kurganov and Tadmor [18], Li, Zhang and Yang [22], among

others. General patterns of shock reflections have been revealed, some cases of which are accessible to analytical treatment. See for instance, the global theory for regular reflection-diffraction for potential flow, established in Chen-Feldman [3],[4],[5] and Bae-Chen-Feldman [1]. For the local stability of the Mach reflection configuration, see Chen [6],[7].

We consider the special case with initial data of piecewise constant solutions joined by four forward rarefaction waves, see Chapter 2. For this case, the solution was conjectured to be continuous, see [2],[28], [20], [22]. This thesis based on [14], in which a transonic shock is discovered through refined numerical simulations and generalized characteristic analysis, and the mathematical mechanism of shock formation for four rarefactions cases is clarified. This transonic shock was omitted in the conjecture [31] and all of the aforementioned numerical simulations in which the total number of genuinely different configurations for adiabatic gas in 2D Riemann problem is 19. To our best knowledge, shock formation in a rarefaction wave-only 2D Riemann problem, had not been previously observed. Gui-Qiang Chen comments [14] in the referee report as follows: "This is breakthrough paper and answers at least numerically one of the major issues in transonic flow: what is the nature of the $M = 1$ line in shock reflection. It turns out the line can contain shocks formed by rarefactions. This is a surprise to me. It will set the tone for further computation and analysis".

1.3 Numerical method

Front tracking is a numerical method which is based on the Riemann solution and Glimm's method. It combines with some effective CFD method, i.e. MUSCL

[10], and provides high resolution for capturing interfaces and discontinuities (shock front) among possibly different component materials. As used here, with no use of tracking, it is a pure CFD method based on MUSCL.

From the point of view of physically motivated wave interactions, arbitrary angles between waves may be considered and special solutions (stationary wave interactions) in general will occur at angles other than 90^o, see [16]. From the point of view of defining a Riemann solution for a finite difference mesh, we might consider a variety of meshes with different angles between the cell edges. In accordance with both points of view, we consider the oblique four-wave Riemann problem. We perform refined numerical experiments, using the FronTier code developed at the AMS department, SUNY Stony Brook and obtain resolved numerical solutions. This code uses a five point vectorized split MUSCL scheme [10] as a shock capturing algorithm. It is second order accurate for smooth solutions and first order accurate near shock waves. We solved the full compressible Euler equations in the original x, y, t coordinates, not in self-similar coordinates, so the numerics are actually very well documented in the literature [10] and [13]. Generalized characteristic analysis in [22] has been developed into a tool for analysis of simulation data in [14] and as presented here. All computations were performed on the Galaxy computer and seawulf computer at Stony Brook and the Stony Brook-Brookhaven New York Blue computer.

1.4 The summary of the thesis work

Our main result is the existence of a shock wave, established numerically by several different criteria, for a 2D Riemann problem with four rarefaction waves in

both the 90 degrees case and the oblique case. The possibility of shock formation indicates the deep sophistication of this seemingly easy problem.

We formulate plausible structures for the solution via the method of generalized characteristic analysis (i. e., the analysis of characteristics, shocks, and sonic curves or the law of causality). In Chapter 2, we study characteristics in the numerical solutions. The existence of shock waves is established by multiple criteria. Specifically, we consider

1. plots of density and pressure on a curve through the shocks;
2. nontangential termination of characteristics at the shock front;
3. convergence of characteristics of the same family at the local shock front;
4. pattern recognition software for automated shock wave detection.
5. stability of above criteria under mesh refinement.

We summarize numerical results for several cases. In Chapter 3, we study the 90^o case and analyze numerical results for shock formation using generalized characteristics analysis. In Chapter 4, we consider the oblique case and prove numerically the convergence of the simulation in the case of a very weak shock. We present related evidence for shock formation in the case of two backward and two forward rarefaction waves. In Chapter 5, we discuss the physical mechanism that leads to the shock formation in the present problem and summarize results testing the stability of the numerical solutions.

Chapter 2

The Problem Formulation and Its Characteristic Curves

In this chapter, we formulate the problem under study and discuss an algorithm for the construction of characteristics in the numerical solutions and summarize fundamental numerical results.

2.1 Oblique four-wave Riemann problem

We consider the Euler equations

$$\begin{aligned} &\rho_t + \nabla \cdot (\rho U) = 0 \ , \\ &(\rho U)_t + \nabla \cdot (\rho U \otimes U) + \nabla p = 0 \ , \\ &(\rho E)_t + \nabla \cdot ((\rho E + p)U) = 0 \end{aligned} \tag{2.1.1}$$

for the variables (ρ, U, E), where ρ is the density, $U = (u, v)$ is the velocity, p is the pressure, $E = \frac{1}{2}|U|^2 + e$ is the specific total energy, and e is the specific internal

energy. We consider a polytropic gas with pressure p defined by the equation

$$e = \frac{p}{(\gamma - 1)\rho} \ .$$

For more details, see the books by Li et. al. [22] or Zheng [32].

We solve the full compressible flow equations (2.1.1) in the original x,y,t coordinates. Our numerical studies are based on (2.1.1), using the MUSCL algorithm [10] as implemented in the FronTier code. This code uses a five point vectorized split MUSCL scheme [10] as a shock capturing algorithm. It is the second order accurate for smooth solutions and the first order accurate near shock waves.

Both the MUSCL algorithm and FronTier code have been extensively verified for shock capturing simulations, for example in [10] and [13]. Shock jump conditions for (2.1.1) can be found in standard textbooks, for example, in [8].

The numerical verification of these jump conditions is addressed in chapter 4. Because the equation (2.1.1) and the initial data are both self-similar, the solution is also, and we introduce the self-similar coordinate system $(\xi, \eta) = (\frac{x-x_0}{t}, \frac{y-y_0}{t})$ centered at the point (x_0, y_0). In these coordinates, the system (2.1.1) takes the form

$$\begin{aligned}
&-\xi\rho_\xi - \eta\rho_\eta + (\rho u)_\xi + (\rho v)_\eta = 0 \ , \\
&-\xi(\rho u)_\xi - \eta(\rho u)_\eta + (\rho u^2 + p)_\xi + (\rho uv)_\eta = 0 \ , \\
&-\xi(\rho v)_\xi - \eta(\rho v)_\eta + (\rho v^2 + p)_\eta + (\rho uv)_\xi = 0 \ , \\
&-\xi(\rho E)_\xi - \eta(\rho E)_\eta + (\rho u(E + \tfrac{p}{\rho}))_\xi + (\rho v(E + \tfrac{p}{\rho}))_\eta = 0 \ .
\end{aligned} \tag{2.1.2}$$

Let $\eta = \eta(\xi)$ be a smooth discontinuity with limit states (ρ_1, u_1, v_1, p_1) and (ρ_0, u_0, v_0, p_0) on both sides. The Rankine-Hugoniot relation for (2.1.2) is derived

in [22, page 218-219]. By definition, Riemann initial data is constant along radial directions from an origin (x_0, y_0) and piecewise constant as a function of angle. The initial data for (2.1.1) become boundary data at infinity for (2.1.2).

We use the self-similar formulation (2.1.2) for the analysis of numerical solutions of (2.1.1). We specialize to a four-rarefaction wave Riemann problem.

As a special case we consider first the case of four rectangularly oriented waves, representing boundary conditions at infinity for the self-similar Euler equations (2.1.2) satisfying conditions of four forward rarefaction waves, denoted configuration A in [22, page 237]. We next consider the case of four constant states joined by forward rarefaction waves that form angles different from 90^o as in Fig. 2.1.1. Such a problem is called *an oblique four-wave Riemann problem*, in contrast to the rectangular four-wave Riemann problem discussed in [31]. Our initial data is located as indicated in Figure 2.1.1 in the initial plane.

$$(\rho, u, v, p) = (\rho_i, u_i, v_i, p_i), \quad i = 1, 2, 3, 4. \tag{2.1.3}$$

2.2 Four forward rarefactions and compatibility condition

Let R_{ij} denote the forward rarefaction wave, which is a 1D rarefaction wave, connecting contiguously constant states (ρ_i, u_i, v_i, p_i) and (ρ_j, u_j, v_j, p_j). R_{12} is parallel to the positive y-axis, and R_{41} is parallel to the positive x-axis as before, but the angle between R_{23} and the negative x-axis is allowed to be a variable θ in $(0, \pi/4)$.

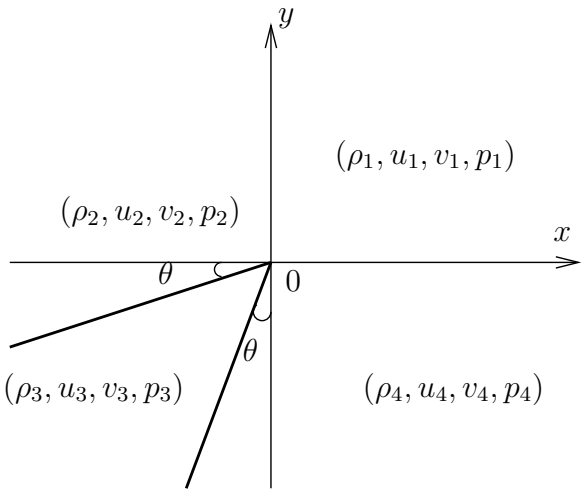

Figure 2.1.1: The initial data for an oblique four-wave Riemann problem

To simplify the analysis, we impose symmetry about the line $x = y$. We choose the angle between R_{34} and the negative y-axis be the same θ, so that the angle between R_{23} and R_{34} is equal to $\frac{\pi}{2} - 2\theta$. Let w represent the velocity component that is perpendicular to the line of discontinuity, and w' represent the velocity component parallel to it. At an interface $(i, j) \in \{(1, 2), (2, 3), (3, 4), (4, 1)\}$, a forward planar rarefaction wave R_{ij} is described by the formula in [20]

$$w_i - w_j = \frac{2\gamma^{\frac{1}{2}}}{\gamma - 1}\left(\left(\frac{p_i}{\rho_i}\right)^{\frac{1}{2}} - \left(\frac{p_j}{\rho_j}\right)^{\frac{1}{2}}\right) , \qquad w_i' = w_j' \, , \frac{p_i}{p_j} = \left(\frac{\rho_i}{\rho_j}\right)^{\gamma} . \tag{2.2.1}$$

For each R_{ij}, the compatibility conditions derived from (2.2.1), using the normal and tangential components of $u_i, v_j, i, j = 1, 2, 3, 4$ along R_{ij}, are

$$(\rho_3^{(\gamma-1)/2} - \rho_4^{(\gamma-1)/2})\cos\theta - (\rho_2^{(\gamma-1)/2} - \rho_3^{(\gamma-1)/2})\sin\theta + (\rho_1^{(\gamma-1)/2} - \rho_2^{(\gamma-1)/2}) = 0 \; ; \tag{2.2.2}$$

$$(\rho_2^{(\gamma-1)/2} - \rho_3^{(\gamma-1)/2})\cos\theta - (\rho_3^{(\gamma-1)/2} - \rho_4^{(\gamma-1)/2})\sin\theta - (\rho_1^{(\gamma-1)/2} - \rho_4^{(\gamma-1)/2}) = 0\ . \quad (2.2.3)$$

We limit ourselves to the initially symmetric case $\rho_2 = \rho_4$ and $u_1 = v_1$. It is proved in [22, page 239] that the solution is symmetric with respect to the line $x = y$. Then the two compatibility conditions merge to yield

$$\rho_2^{(\gamma-1)/2}(\cos\theta + \sin\theta + 1) = \rho_1^{(\gamma-1)/2} + \rho_3^{(\gamma-1)/2}(\sin\theta + \cos\theta)\ . \quad (2.2.4)$$

For any fixed $\rho_1, p_1, u_1, v_1, \rho_3$, and θ, we find ρ_2 from the compatibility condition (2.2.4) and other initial values from (2.2.1) and symmetry. We consider a fixed polytropic index $\gamma = 1.4$. The computational domain is a square $[0,1] \times [0,1]$. We perform numerical experiments with varying Riemann initial data.

2.3 Characteristics and its algorithm

We draw both families of (pseudo) characteristic curves corresponding to $\lambda_\pm$ in [22],

$$\frac{d\eta}{d\xi} = \lambda_\pm(\xi,\eta) \equiv \frac{(u-\xi)(v-\eta) \pm c[(u-\xi)^2 + (v-\eta)^2 - c^2]^{1/2}}{(u-\xi)^2 - c^2}\ , \quad (2.3.1)$$

where c is the sonic speed, $\xi = \frac{x-x_0}{T_0}, \eta = \frac{y-y_0}{T_0}, T_0$ is fixed, and $x_0 = y_0 = 0.5$ is the center of the computational domain. By the definition in [22], the pseudo-Mach

number is

$$M = \frac{[(u-\xi)^2 + (v-\eta)^2]^{1/2}}{c} \ . \tag{2.3.2}$$

The $M = 1$ contour, as understood here, indicates both sonic points and shock points, where M jumps from a value less than 1 to a value greater than 1. The sonic curve is thus a subset of the $M = 1$ contour line. We notice $\lambda_+ = \lambda_-$ on the sonic curve.

We discuss the algorithm for characteristics. The characteristic curves starting at the top boundary of the rectangular domain belong to the family λ_+, while the characteristic curves from the right boundary of the rectangular domain belong to λ_-.

To draw the $\lambda_\pm$ characteristics, we assume the numerical solution of the Euler equations is defined on a rectangular grid. We extend this solution to the entire computational domain ξ, η plane for a discrete time $t = T_0$, using linear interpolation. Thus $\lambda_\pm$ become globally defined functions. Starting at the the right boundary, we solve for λ_- to obtain the pseudo characteristic curves, using the Runge-Kutta scheme. The solution for λ_- terminated on the $M = 1$ contour line is continued up to the sonic curve. For the reflected characteristics $\lambda_\pm(\xi, \eta)$ at the sonic curve, we repeat the above processes. Since these characteristics are reflections of the previously constructed family, we use bilinear interpolation to obtain initial states at the point on the $M = 1$ contour where an incoming characteristic has terminated. For instance, for the reflected characteristics $\lambda_+(\xi, \eta)$, we first use bilinear interpolation and to obtain the corresponding states of the known sonic point in the local grid. Then we use the Euler method and obtain the reflected point of the characteristics, such that both of

the point and sonic point are in the same grid cell. We solved all singularities in the characteristics equations (2.3.1) numerically.

2.4 Numerical shock criteria

Since the main point of this paper is to establish the existence of a shock wave, we list here criteria that we use for this purpose.

The most sensitive of our measures for existence of a shock wave is the fact that a shock will appear when the two families of $\lambda_{\pm}$ characteristics are not parallel at the $M = 1$ contour line. The existence of a point on the $M = 1$ contour line with λ_+ not parallel to λ_- contradicts (2.3.1) if the point on the $M = 1$ contour is a sonic point, i.e. a point at which the solution is continuous. Several different types of plots are used in this confirmation. We thus plot $\lambda_- - \lambda_+$ vs. the angle around $M = 1$ contour, where the shock is identified as the locus of points on the contour with $\lambda_- - \lambda_+ > 0$. The end points of the shock are identified relative to figures showing characteristics.

A second test for existence of a shock is to show convergence of nearby characteristics of a common family, so that they meet on the $M = 1$ contour. As a third test, we plot ρ vs. distance along a streamline. By definition in [22], pseudo-stream curves satisfy $\frac{d\eta}{d\xi} = \lambda_0 = \frac{v-\eta}{u-\xi}$. The solution to (2.1.1) is called a compression wave if $(1, u, v) \cdot (\rho_t, \rho_x, \rho_y) > 0$; otherwise it is called expansion wave. We notice the fact

$$(u - \xi, v - \eta) \cdot (\partial_\xi, \partial_\eta) = t(1, u, v) \cdot (\partial_t, \partial_x, \partial_y) = t\frac{d}{dt}, \tag{2.4.1}$$

where $\frac{d}{dt}$ is evaluated along the trajectories of gas particles in (t, x, y)-space. All

pseudo-stream curves point to the center of subsonic domain. Moreover, we have

$$\begin{aligned}
\frac{d\rho(\xi,\eta)}{dt} &= \frac{\partial\rho}{\partial\xi}\cdot\frac{\partial\xi}{\partial t}+\frac{\partial\rho}{\partial\eta}\cdot\frac{\partial\eta}{\partial t} \\
&= \frac{\partial\rho}{\partial\xi}\cdot\left(\frac{\partial\xi}{\partial x}\frac{dx}{dt}-\frac{x}{t^2}\right)+\frac{\partial\rho}{\partial\eta}\cdot\left(\frac{\partial\eta}{\partial y}\frac{dy}{dt}-\frac{y}{t^2}\right) \\
&= \frac{\partial\rho}{\partial\xi}\cdot(\frac{u}{t}-\frac{\xi}{t})+\frac{\partial\rho}{\partial\eta}\cdot(\frac{v}{t}-\frac{\eta}{t}) \\
&= \frac{1}{t}\,(u-\xi,v-\eta)\cdot(\rho_\xi,\rho_\eta) \\
&= \frac{1}{t}\frac{d\rho(\xi,\eta)}{ds}\ ,
\end{aligned}$$

where in the last term, $\frac{d\rho(\xi,\eta)}{ds}$ is the directional derivative of the density ρ along the pseudo-stream curve. According to (2.4.1), a positive value for this derivative indicates a compression or a shock, and a jump indicates a shock. We also plot pressure along a ray passing through the $M = 1$ contour. A sharp jump in pressure is a sign of a possible shock. Finally, we use the wave detection filter, or automated shock detection capability in the FronTier code to locate shock waves in [30]. This software examines numerical discontinuities in the solutions and determines whether they correspond to a particular type of traveling wave. Such discontinuities are organized into curves, which then correspond to the location of a shock wave. The shock jump conditions are included in the Rankine-Hugoniot relation. These jump conditions are verified to confirm that the shock waves detected by the wave filter indeed satisfy the required conditions. Numerical solutions show stability of the above shock criteria under mesh refinement.

2.5 Two shock formation mechanisms

Our major point is the consistency of these tests, each reaching the same conclusion: shocks exist in the interior non-constant domain in the 2D rarefaction Riemann problems studied here. We find two distinct mechanisms for shock formation. For the 90^o case, the interaction of two rarefaction waves, of the same family and parallel at infinity leads to a pressure drop larger than that due to either taken singly. Thus the interaction seems to 'over rarefy', leading to low pressure states incompatible with pressures given at infinity due to the same rarefactions considered individually. A shock wave results from the joining of these high and lower pressure regions. It is the interaction of rarefaction R_{41}, R_{23}, R_{34} and R_{12}, including the interaction of characteristics from constant states adjacent to them, which produce this result. A second mechanism arises in the case of a (sufficiently) large oblique angle between the rarefaction waves. In this case, the rarefactions R_{41} and R_{12} are followed by a reflected simple wave, coming off the sonic curve, reflected from the sonic curve. The sonic curve has extended ears to facilitate this reflection. The reflected wave becomes a compression and breaks into a shock at the $M = 1$ contour, at points that would otherwise be sonic, but actually lie on a shock front. The solution is jointly determined by the subsonic domain and the supersonic domain. The numerical results indicate that this reflected simple wave along the sonic curve is a compressive wave and forms a shock eventually.

Table 2.1: Table of simulation cases studied in this thesis

Three cases	90^o	weakly oblique rarefaction	oblique rarefaction
initial conditions	$\rho_1 = 1.0, p_1 = 0.444, u_1 = v_1 = 0.0, \rho_3 = 0.15$		
θ values	$\theta = 0^o$	$6^o \leq \theta \leq 8^o$	$\theta > 8^o$
Shock case	Weak shock	Weak shock	Shock
Mesh Size $\Delta x = \Delta y$	$\frac{1}{3200}, \frac{1}{1600}$	$\frac{1}{5600}, \frac{1}{3200}, \frac{1}{1600}, \frac{1}{800}$	$\frac{1}{800}$

2.6 Summary of numerical simulations

We introduce our further refined numerical results this section. When the four-waves form angles close to or equal to 90^o, our calculations show shocks in the solutions. We use the method of generalized characteristic analysis to indicate the plausible structure of the solution for both $\theta = 0$ and $\theta > 0$, confirming theoretical conjectures regarding the mechanisms for shock formation. We fix the computational time $T_0 = 0.375$ and let the initial values be p_1, ρ_1, $u_1 = v_1 = 0$, ρ_3 and determine all initial values with different θ. We list the cases to be considered in Table 1. We denote by $C_i(u_i, v_i, c_i)$, $i = 1, 2, 3, 4$, the sonic circles of constant states i, $i = 1, 2, 3, 4$, where u_i, v_i, $i = 1, 2, 3, 4$, are initial velocities and $c_i = \left(\frac{\gamma p_i}{\rho_i}\right)^{\frac{1}{2}}$, $i = 1, 2, 3, 4$, are initial sound speeds.

A. Weak shock case for $\theta = 0$ (90^o case)

The 90^o case is shown in Fig. 2.6.1 with results consistent with on both coarse and refined grids. The λ_--characteristic lying at the upper boundary of R_{41} coming from infinity penetrates the rarefaction wave $R_{12}(CQ)$, and continues through the constant state 2 (QR) and the rarefaction wave $R_{23}(RF)$, reaching the constant state 3, and meets the sonic circle $C_3(u_3, v_3, c_3)$ tangentially at A. See the strict proof in [22, page 238]. The bottom boundary of R_{23} (FT) hits the $M = 1$ contour at T. The

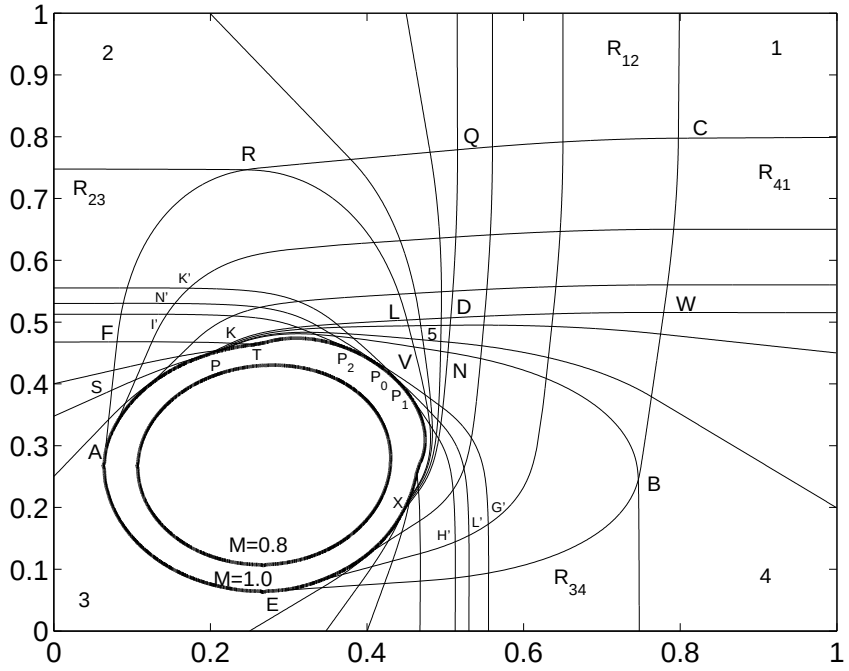

Figure 2.6.1: Case A: Some pseudo-characteristic curves (light) and Mach number contours (bold) marked with $M = 1.0$ and $M = 0.8$ at $\theta = 0$.

top boundary of $R_{23}(RV)$ hits the $M = 1$ contour at X and a weak shock appears on the larger arc AE (toward the first quadrant), where A, E are symmetric points relative to reflection about the axis $\xi = \eta$.

The smaller arc AE (toward the third quadrant) is an arc of the sonic circle C_3. Numerical evidence supports weak shocks on both sides of the sonic circle. The shocks and the numerical evidence for them are stronger on the side nearer the origin. We will discuss these points in detail later.

B. Weak shock case: numerical solutions with $\theta \in [6^o, 8^o]$

We use generalized characteristics analysis and refined numerical evidence, ob-

taining weak shock cases for $\theta \in [6^o, 8^o]$. The cases $\theta = 6.5^o$ and $\theta = 8^o$ will be discussed in detail. See Fig. 2.6.2 and Fig. 4.1.7 for the cases $\theta = 6.5^o$ and $\theta = 8^o$. In Fig. 2.6.2, both the upper boundaries FS of R_{41} and GS of R_{23} are parallel, tangential to the sonic curve at S. SA is tangential to the sonic circle C_3 at A, which is a reflection of the λ_+-characteristic curve GS. SK, which is the reflection of the λ_--characteristic curve FS, terminates on a shock. The weak shock appears on the arc $AT \bigcup BR \bigcup UE$, where A, E are symmetric points regarding the axis $\xi = \eta$, and the smaller arc AE is the arc of sonic circle C_3.

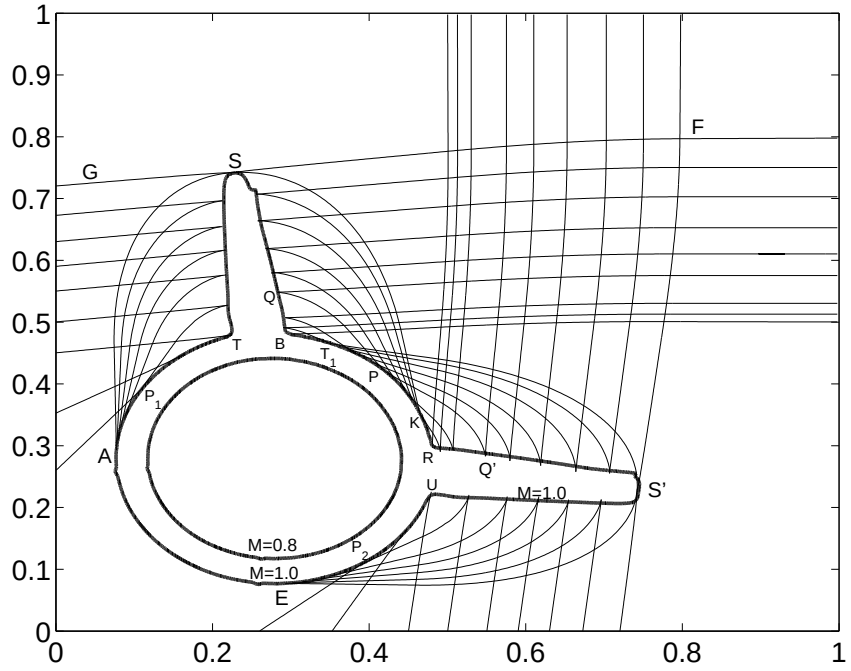

Figure 2.6.2: Case B: Some pseudo-characteristic curves (light) with $\theta = 6.5^o$ and Mach number contours (bold) marked with $M = 1.0$ and $M = 0.8$.

C. Strong shock case: numerical solutions with $\theta > 8^o$

We increase the value of θ, and we observe a shock wave which is sharply defined and with little numerical oscillation. The shock wave lies in the interior, non-constant domain between R_{23} and R_{34} and constant states adjacent to them whose structure is similar to case B. See Fig. 2.6.3. Furthermore, we find that the strength of the shock wave becomes stronger as we increase θ or decrease ρ_3 while keeping the other parameters constant. The numerical oscillations between R_{23} and R_{34} attenuate, or even vanish as the strength of the shock wave intensifies. In summary, numerical solutions show the existence of shock waves in the interaction of four rarefaction waves and constant states.

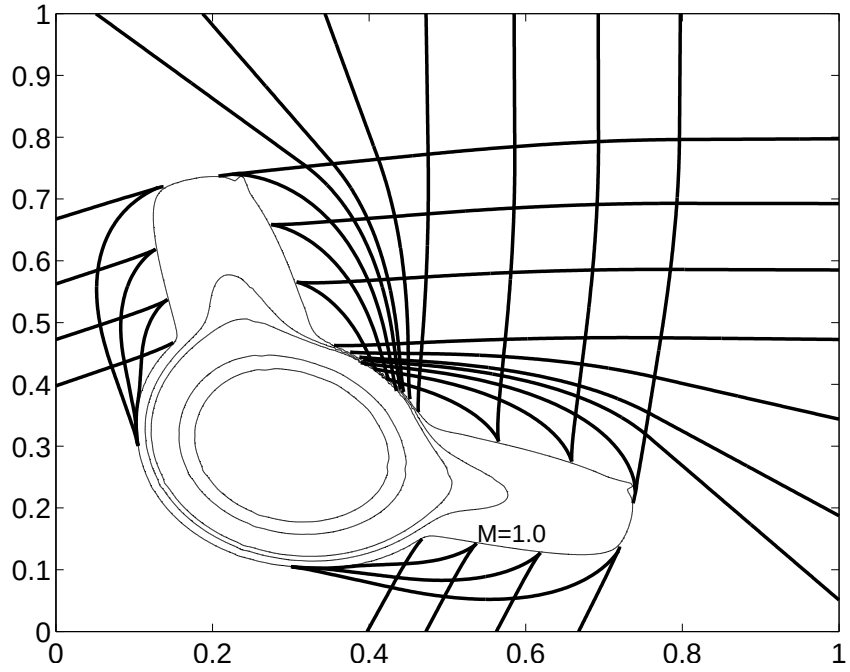

Figure 2.6.3: Case C: Some pseudo-characteristic curves (bold) with $\theta = 22.5^o$ and Mach number contours (light) with the sonic curve labeled $M = 1.0$.

Chapter 3

Shock Formation in the 90^o Case

A constructive analysis of some of the major ideas of this paper is found in [15], where we study the Riemann problem for the Hamilton-Jacobi equations as a simpler problem, developing a number of ideas needed here. These equations can be regarded as a generalization of Burgers' equation to high dimensions. The analysis there follows a constructive point of view, and thus emphasizes ideas such as generalized characteristics, the propagation of the Riemann solution inward from data located at infinity, and a sonic curve as discussed in the present paper.We discuss in this section the shock formation in the 90^o case. We analyze the mechanism for shock formation caused by the interaction of rarefaction waves R_{12}, R_{23}, R_{34} and R_{41}, including the interaction of R_{41} and characteristics from constant state $3, 4, 5$ adjacent to them. We use numerical methods and generalized characteristic analysis.

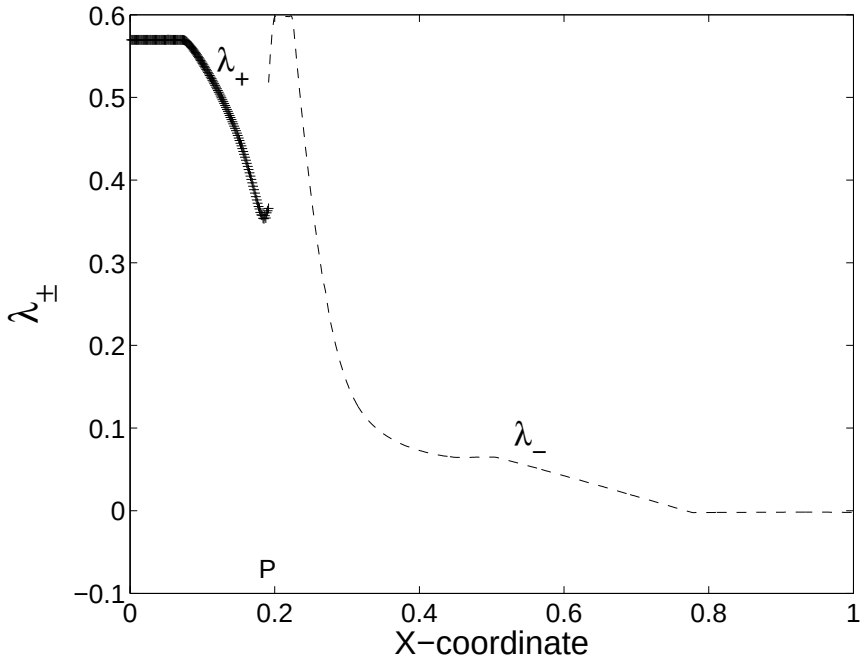

Figure 3.1.1: The characteristics $\lambda_+ = \frac{d\eta}{d\xi}$ along SP and $\lambda_- = \frac{d\eta}{d\xi}$ along WP meet at P. Note that $\lambda_+ \neq \lambda_-$ at the common point P.

3.1 A numerical study of the 90^o case

In Fig. 2.6.1, the characteristic WP along bottom boundary of R_{41} meets the characteristics SP from constant state 3 at P. The intersection point P is located on the $M = 1$ contour. If P were a sonic point, then we would have $\lambda_+(P) = \lambda_-(P)$. However, we show numerically in Fig. 3.1.1 and Fig. 3.1.2 that P cannot be a sonic point because the characteristics are not parallel at P. The numerical results in Fig. 3.1.1, show that at the common point P of the two characteristic curves, $\lambda_+(P) < 0.4, \lambda_-(P) > 0.5, \lambda_+(P) \neq \lambda_-(P)$, indicating that P is not sonic. Thus the termination of the λ_+ characteristic and the beginning of the λ_- characteristic

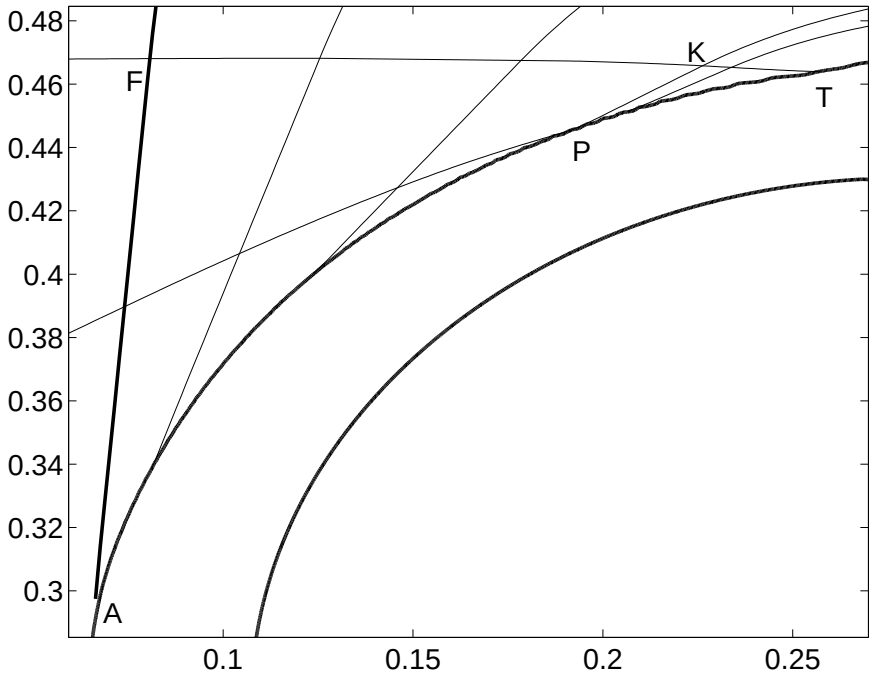

Figure 3.1.2: Enlarged view from Fig. 2.6.1 in the 90^o case shows the non parallel termination of characteristics on the $M = 1.0$ contour (outer curved arc) and shock existence at the point P. Lower curved arc is the $M = 0.8$ contour.

must lie on a shock curve. We have two characteristics $N'P_0$ and $L'P_0$ meet at P_0 on $\xi = \eta$, but they are not parallel. Similarly, $G'P_2$ and $I'P_2$ meet at P_2 nontangentially, $H'P_1$ and $K'P_1$ meet at P_1 nontangentially. P_0, P_1, P_2 are located on a shock front. An enlarged view of the non tangential, non parallel termination of the characteristic curves at the shock front is shown in Fig. 3.1.2. We plot pressure vs. the distance $R = (x^2 + y^2)^{\frac{1}{2}}$ along the straight line OP in Fig. 3.1.3, where O is the center of subsonic domain in $[0, 1] \times [0, 1]$. The downward jump in the pressure is a shock front, and P is shown in Fig. 2.6.1. The curve indicates values at individual mesh points mean the shock. The crosses marked along this plot indicate pressure values

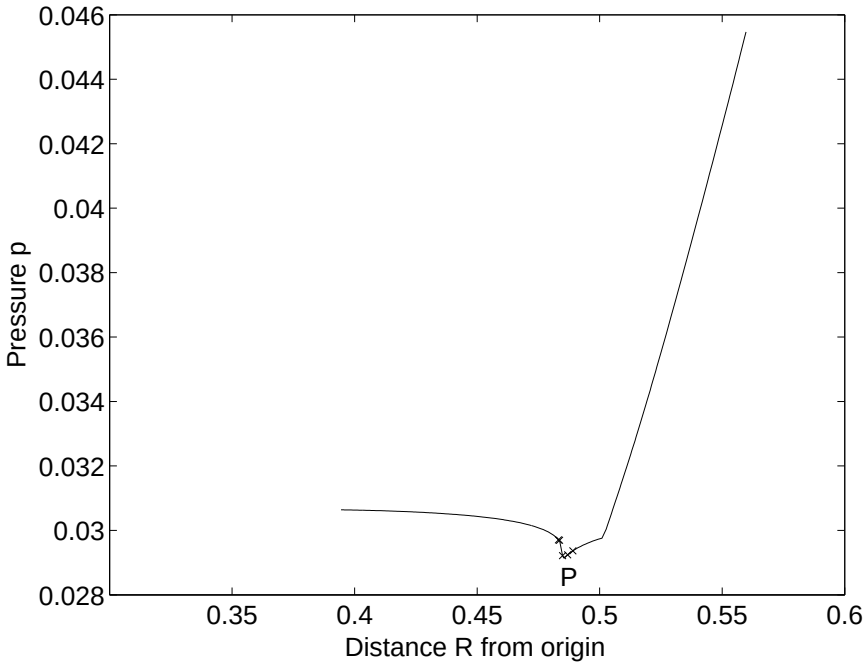

Figure 3.1.3: Pressure vs. distance along OP for the 90^o case. The downward jump at the point P is a shock front. The crosses mark cell center locations near the shock front.

at individual mesh points along the curve, in a neighborhood of the shock. They serve to show that the shock front jump is about one mesh block wide, as is typical for a numerically captured shock. In Fig. 3.1.4, we represent shock strength by the difference in characteristics $\lambda_-(X) - \lambda_+(X)$ vs. the angle plotted along the $M = 1$ contour to show shock existence. The angle between the ray from O and the positive x-axis is denoted by ϕ.

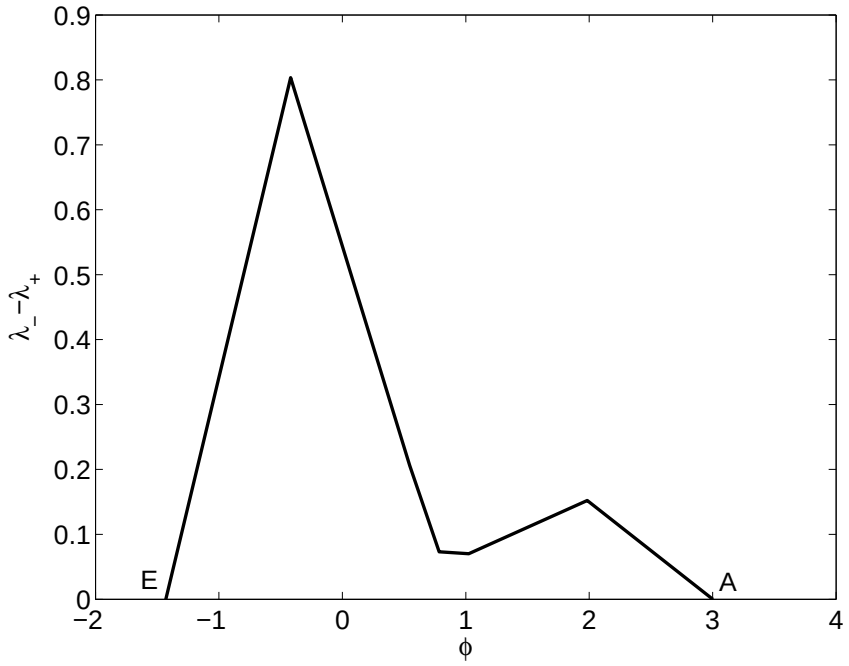

Figure 3.1.4: $\lambda_- - \lambda+$ vs. the angle ϕ along the $M = 1$ contour in the 90^o case. This plot shows the shock existence, and the endpoints E and A of the shock wave shown in Fig. 2.6.1

3.2 Generalized characteristic analysis in the 90^o case

Let us recall [31]. We use the method of generalized characteristic analysis to indicate the plausible structure of the solution in the 90^o case. As in [31], we transform the problem (2.1.1) and (2.1.3) into a boundary value problem. The values imposed at infinity are given by (2.1.1) for the self-similar system (2.1.2).

$$\lim_{\xi^2+\eta^2\to\infty} (\rho, u, v, p)(\xi, \eta) = (\rho_i, u_i, v_i, p_i) \ , \quad i = 1, 2, 3, 4, \tag{3.2.1}$$

in which the limiting direction is consistent with the data sector in (2.1.3). Thus we first construct the solution in the far field (in a neighborhood of the infinity), which is comprised of four forward planar rarefaction waves R_{12}, R_{23}, R_{34} and R_{41}, besides the constant states (ρ_i, u_i, v_i, p_i), $i = 1, 2, 3, 4$. We extend the four forward rarefaction waves inward from the far field till they interact, denoted by regions in Fig. 2.6.1. We find the boundary of the interaction domain, which consists of $CQRFSAEBWC$ in Fig. 2.6.1, where the arc AE is an arc of sonic circle C_3 and K is the intersection point of the bottom boundaries of R_{23} and R_{41}.

Then we solve the first Goursat problem with characteristic segments CQ and CW, employing the result in [21, 24], and obtain a continuous (pseudo-supersonic) solution inside the domain enclosed by the characteristic segments CQ, QD, DW and WC. Secondly, we solve the Goursat problem with characteristic segments QR and QD. The solutions are still continuous in the domain $QRLD$. We continue solve the third Gousat problem with support DL and DN. In [23], they are straight support. Then we get the continuous solutions in the domain $DLVN$. The wave R_{41} penetrates R_{12} and then R_{23} to emerge as a simple wave $RFKL$ by [23], which is adjacent to the constant state 2 and constant state 5 and located in the supersonic domain without shock wave.

We prove rigorously that two subcases possibly happen: either P_3 is greater than P_5 or P_5 is greater than P_3 in [24], where P_3 and P_5 are pressures in constant state 3 and 5. This inverted pressure profile $P_3 > P_5$ is surprising, because one would expect that pressure would be expansive in the interaction of four forward rarefaction waves. However, the inverted pressure profile is the direct result of the interaction of two

waves R_{41} and R_{12}. Why is the pressure drop in the interaction region larger than the combined drop across each of the individual waves? Intuitively or based on physics, it is not easy to see whether the pressure would go up along a characteristic curve to end on a sonic point, or go down to zero to end on a vacuum. In [24], it has been proven rigorously that the pressure in the interaction region approaches zero along any characteristics, which form a hyperbolic domain determined completely by the data on the characteristic boundaries. Once the participating rarefaction waves are relatively large, the binary interaction will produce vacuum, which has been proved rigorously in [24]. The pressure whose initial states satisfies $P_1 > P_2 = P_4 > P_3$ and continues to drop in the simple wave interaction zone $RFKL$, which is proved in [22], to result in an even lower pressure value at K, where K is shown in Figs. 2.6.1 and 3.1.2. From the numerical results, we note that the sonic boundary AP is a free boundary, as the hyperbolic domain of determinacy of the Goursat problem AFT does not include AP, see Fig. 3.1.2. Thus the elliptic region influences the solution there. Numerical results show that a global minimum for the pressure in the whole space $[0,1] \times [0,1]$ occurs in the domain KPT. The high pressure in the subsonic domain, adjacent to the low pressure in the neighboring domain KPT and FAT, forces the shock wave to occur.

Fig. 3.2.1 and Fig. 3.2.2 show the variation of density ρ along the pseudo-stream curve I, and the shock wave caused by compression waves with high pressure in the subsonic domain pushing the expansion wave in the supersonic domain. In Fig. 3.2.2, s denotes the distance along pseudo-stream curve.

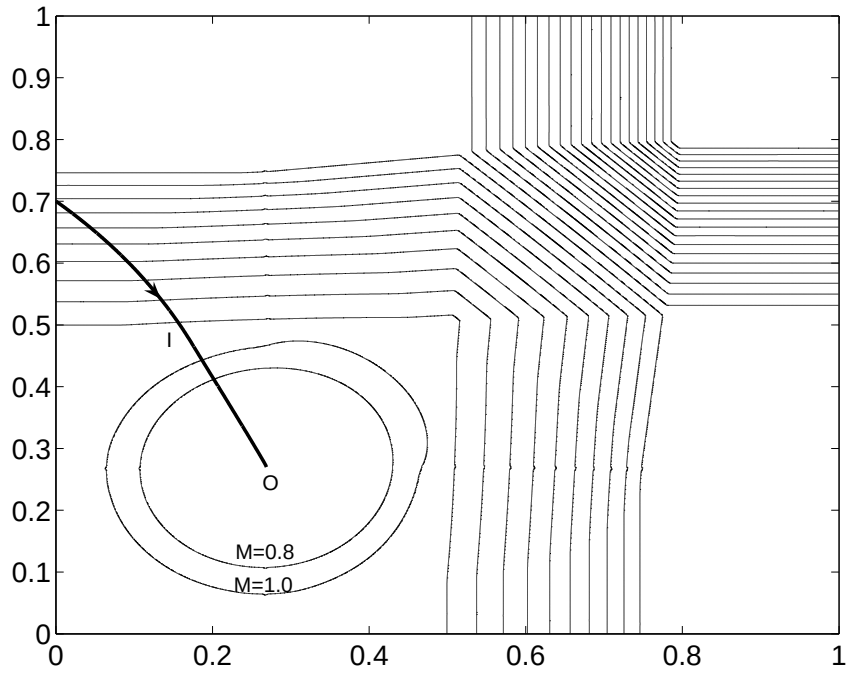

Figure 3.2.1: Density contours (light), two Mach contours (light) with $M = 1.0$ and $M = 0.8$ and pseudo-stream curve I (bold) which cuts through a shock wave in a neighborhood of the $M = 1$ contour. Arrows indicate the direction of particles motion along the stream line.

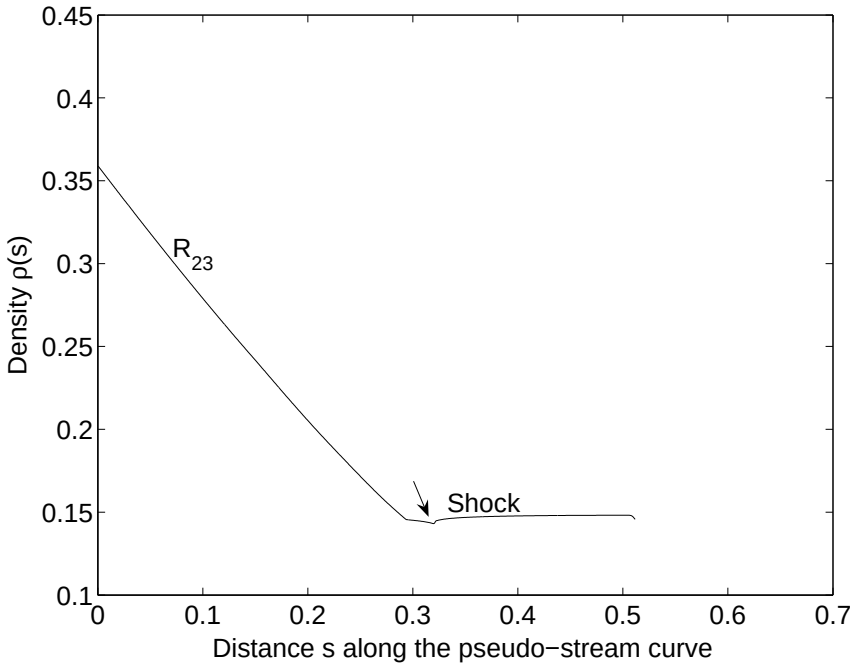

Figure 3.2.2: Plot of $\rho(s)$ vs. s. The position of a shock wave is visible as a small increasing bump with the distance along the pseudo-stream curve I in Fig. 3.2.1.

Chapter 4

Shock Formation in the Oblique Rarefaction Case

We discover the shock formation in the four forward rarefactions in oblique four-wave Riemann problem.

4.1 Numerical results

In oblique wave interaction case at $\theta = 6.5^o$, two reflected characteristic curves $QP, Q'P$ in Fig. 4.1.1, meet at $P|_{X=0.42}$ on the 45^o diagonal line. The intersection point P is located on the $M = 1$ contour. If P were a sonic point, then we would have $\lambda_+(P) = \lambda_-(P)$. However, we show numerically in Fig. 4.1.1 that P cannot be a sonic point because the characteristics are not parallel at P. At the common point P of the two plots, $\lambda_+(P) < -1, \lambda_-(P) > -1, \lambda_+(P) \neq \lambda_-(P)$, indicating that P is not sonic. Thus the termination of the λ_+ characteristics and the beginning of the λ_- characteristics must be on shock. The plots for two computations, showing level of mesh refinement, are indistinguishable. In Fig. 4.1.2, we show shock strength by the difference $\lambda_-(X) - \lambda_+(X)$ in the direction of characteristics vs. the angle around

the $M = 1$ contour. See Fig. 2.6.2 for locations of the points A, T, B, R, U, E. The plot demonstrates shock existence. The angle between the ray from O (the center of subsonic domain) and the positive x-axis is denoted by ϕ. We show further details of the non tangential termination of the characteristic curves at the shock front in Fig. 4.1.3. The characteristic curves terminate non tangentially and are not parallel to each other. We find numerically that the reflected simple wave is a compressive wave and forms a weak shock. See Fig. 4.1.4, where the characteristic distance denotes the 'shock distance'. The separation distance, i.e. the normal separation between two neighboring characteristics is plotted vs. the length along the reflected characteristics. The computed result with mesh refinement demonstrate that The plot also shows the occurrence of the shock.

We plot pressure p vs. the distance from the origin R= $(x^2 + y^2)^{\frac{1}{2}}$ along the 45^o diagonal line in Fig. 4.1.5 and as well as Fig. 4.1.6. Under refinement of the mesh, the oscillations are getting weaker and the shock becomes sharper. The circles and crosses are located at mesh block centers, for cells within the shock profile. The trend of convergence of shocks in each plot in Fig. 4.1.5 is clear and sufficient: the shock wave here is very weak but its strength is not decreasing as mesh is refined; the shock will be stable even with extremely fine meshes.

We use the wave filter embedded in the FronTier code. The wave filter is an automated pattern recognition algorithm which locates shock waves, rarefaction waves and contact discontinuities in numerical solutions of the Euler equations for compressible fluids on the basis of detecting a local jump in the solution which satisfies the Rankine-Hugoniot relations. The shock wave as determined by this wave filter

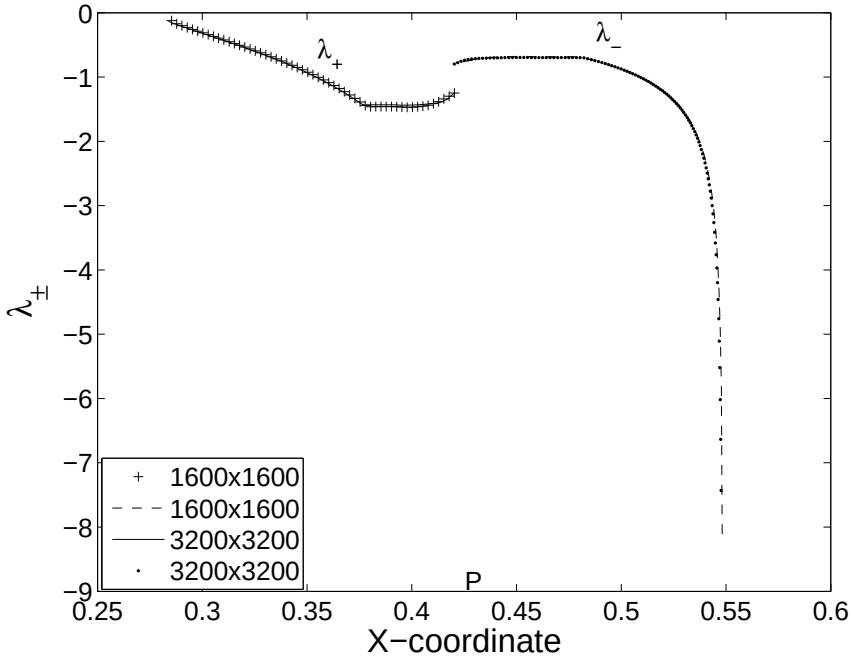

Figure 4.1.1: Plot of $\lambda_+ = \frac{d\eta}{d\xi}$ along QP and $\lambda_- = \frac{d\eta}{d\xi}$ along PQ' show the shock existence at P, since $\lambda_+(P) \neq \lambda_-(P)$. The plots for two computations, showing one level of mesh refinement, are indistinguishable.

program is shown in Fig. 4.1.7 by the curve AB. Note that the labeled Mach number contours $M = 0.98$ and $M = 1.02$ in Fig. 4.1.7 and $M = 0.96$ and $M = 1.02$ in Fig. 4.1.8 coincide on the curve AB respectively, indicating that they are shock fronts. These curves match the pseudo-Mach number contours well.

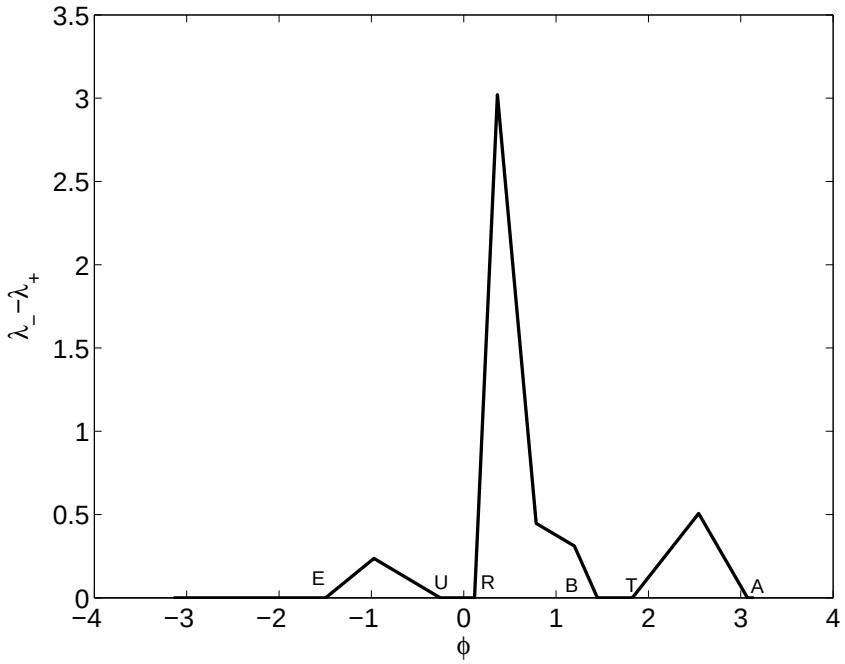

Figure 4.1.2: The difference $\lambda_-(X) - \lambda_+(X)$ vs. angle along the $M = 1$ contour at $\theta = 6.5^o$. This plot shows existence of shocks on both sides of the $M = 1$ contour, i.e. the state facing the origin and facing infinity in the fourth quadrant.

4.2 Generalized characteristic analysis for shock formation in oblique rarefaction case

We use the method of generalized characteristic analysis to indicate the plausible structure of the solution to our problem for $\theta > 8^o$ based on numerical results in Section 4.1. We retain the notation from [31]. We discuss causal relationships and decompose the boundary value problem into three sub-problems based on the features of the characteristics. The analysis consists of the following steps. The first is a classical rarefaction Goursat problem which has been solved analytically in [21, 24].

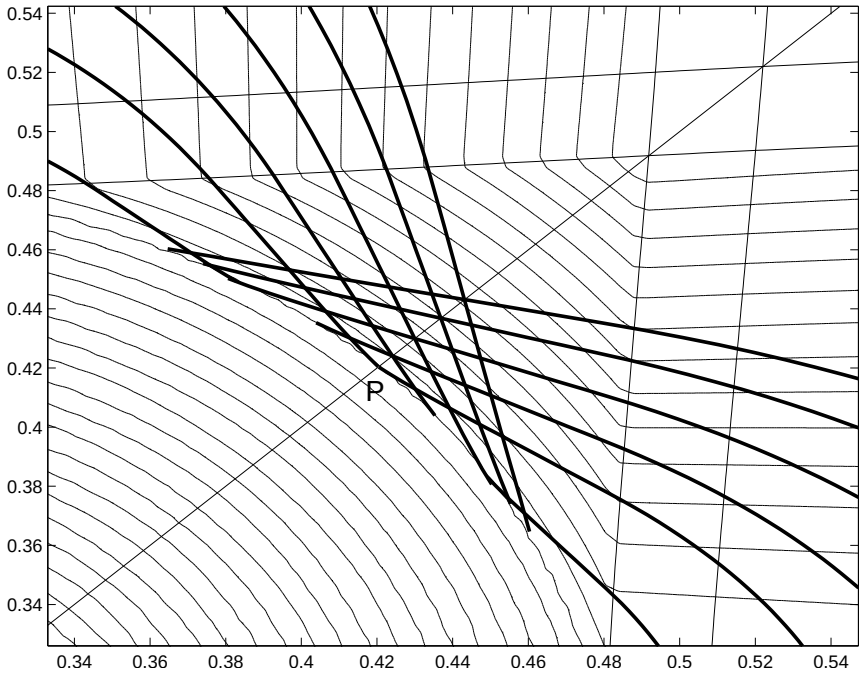

Figure 4.1.3: Enlarged view with details in Fig. 2.6.2 near the point P on the shock front. Bold curves are $\lambda_{\pm}$ characteristics; light curves are Mach number contours. Note that the characteristics terminate non tangentially on the shock.

The second is a degenerate Goursat problem, whose solution is proved to be a simple wave in [23]. The last is a pseudo-transonic boundary value problem with free boundaries consisting of interior sonic curves and shocks. The mathematical proof for the structure of this last sub-problem is open. The problem involves collisions of rarefaction waves with sonic curves which produce compressive waves upon reflection, which may then form shocks. We outline the boundary of the domain of interaction for the initial four rarefaction waves in both cases above.

Step 4.2.1. The constant states and simple waves in the far field.

As in [31], we transform problem (2.1.1) and (2.1.3) into a boundary value prob-

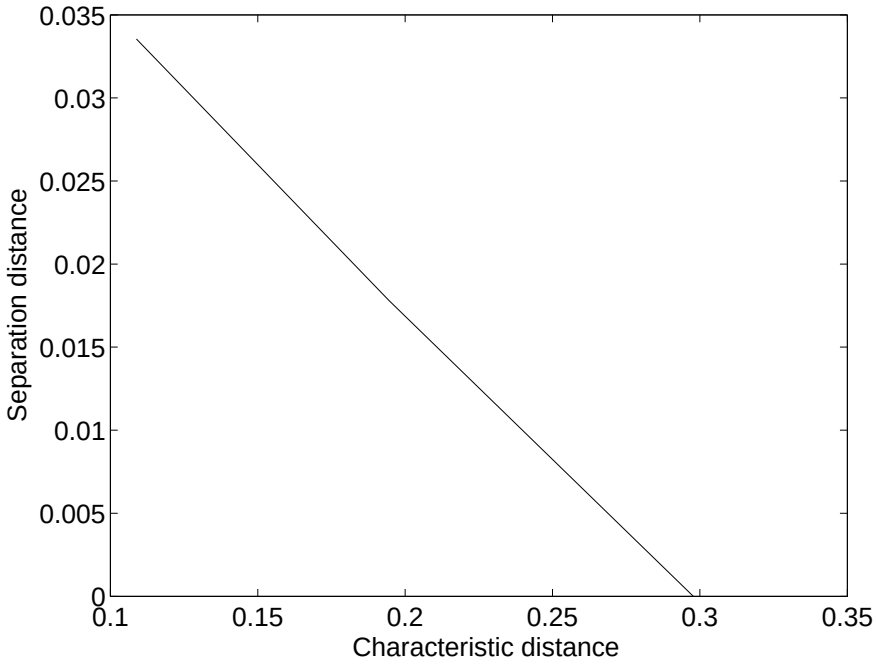

Figure 4.1.4: Plot of separation between neighboring characteristics vs. distance along characteristics with $\theta = 6.5^o$ in case B. This plot shows shock formation.

lem for the self-similar system (2.1.2) with values imposed at infinity

$$\lim_{\xi^2+\eta^2\to\infty}(\rho,u,v,p)(\xi,\eta)=(\rho_i,u_i,v_i,p_i)\ ,\quad i=1,2,3,4, \tag{4.2.1}$$

in which the limiting direction is consistent with the data sector in (2.1.3). We first construct the solution in the far field (neighborhood of the infinity), which is comprised of four forward planar rarefaction waves R_{12}, R_{23}, R_{34} and R_{41}, besides the constant states (ρ_i, u_i, v_i, p_i), $i = 1, 2, 3, 4$. We extend the four forward rarefaction waves inward from the far field till they interact, denoted by regions as in Fig. 4.2.1. We find the boundary of the interaction domain, as in [31], which consists of the

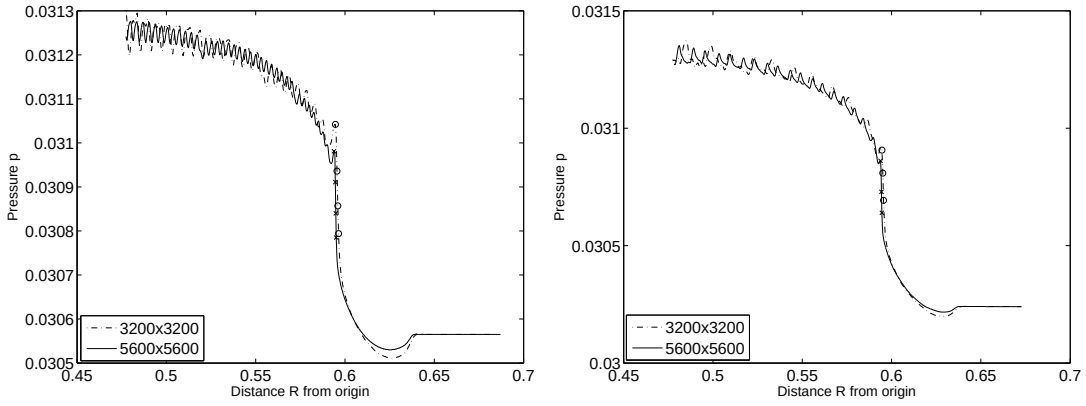

Figure 4.1.5: Left: pressure vs. distance along a 45^o diagonal line at 6^o. Right: pressure vs. distance along a 45^o diagonal line at $\theta = 6.5^o$. The x and o indicate cell center solution values moving through the shock, for the region of rapid solution transition.

characteristic segments PQ, QR, ST, TU, $U'T'$, $T'S'$, $R'Q'$, $Q'P$ and arcs of sonic circles RS, UU', $S'R'$. See Fig.4.2.1.

Step 4.2.2 Simple wave solutions after interaction of planar rarefaction waves.

The two rarefaction waves R_{12} and R_{41} start to interact at P. We use the result in [21, 24] to solve the Goursat problem with the boundary values supported on the characteristic curves PQ and PQ', and obtain a continuous (pseudo-supersonic) solution inside the domain enclosed by the characteristic segments PQ, QP', $P'Q'$ and $Q'P$. Then we proceed to solve the Goursat problem with the boundary data supported on QR and QP'. Since the state (ρ_2, u_2, v_2, p_2) is constant, we use the result in [23, Theorem 7]: *Adjacent to a constant state is a simple wave in which* (ρ, u, v, p) *are constant along a family of wave characteristics which are thus straight.*

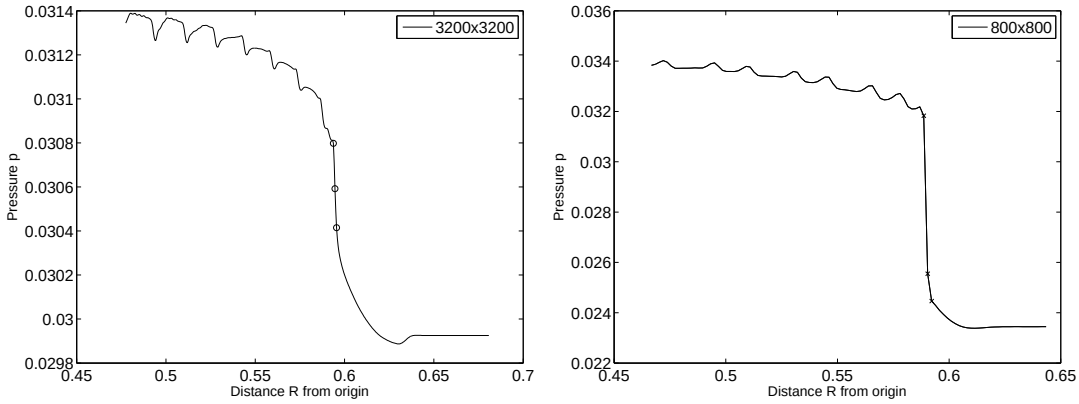

Figure 4.1.6: Pressure vs. distance along a 45^o diagonal line. Left: $\theta = 7^o$. Right: $\theta = 22.5^o$

This fact indicates that the solution is a simple wave, denoted by R_{25}, in the angular domain between QR and QP'.

We note that the simple wave R_{25} just covers the region of the curvilinear quadrilateral $QRWP'$ from the theory of characteristics, where RW is the λ_+-characteristic curve from the point R and can be regarded as the reflection of the λ_--characteristic curve at that point. Also note that the point R on the sonic curve C_2 is degenerate. It has the following interesting properties: It is of Tricomi type from the side of R_{25}, but of Keldysh-type from the side of the constant state (ρ_2, u_2, v_2, p_2). A point on a sonic curve is said to have a Tricomi type if the characteristics are non-tangential to the sonic curve. It is called Keldysh type if the characteristics are tangential to the sonic curve.

We continue to solve the Goursat problem with the support of two straight characteristic curves $P'W$ and $P'W'$. Obviously, the solution is a constant state (ρ_5, u_5, v_5, p_5) with boundary $P'WXW'$. The point X must be outside the sonic

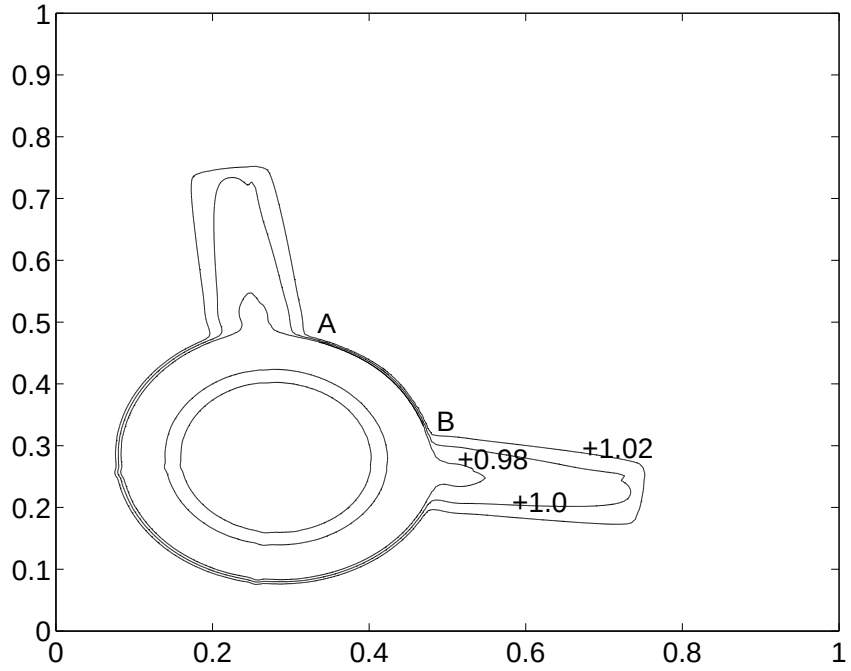

Figure 4.1.7: Comparison of wave filter shock location A, B and pseudo-Mach number contour plots at $\theta = 8^o$ with 800×800 mesh.

circle of the state (ρ_5, u_5, v_5, p_5).

Step 4.2.3 Plausible solution structure in intersecting supersonic regions with the transonic boundary.

After the above three Goursat problems, we reach the boundary $RWXW'R'$. Now we consider a the problem of the pseudo transonic flow with the boundary $RSTUU'T'S'R'W'XWR$. It is reasonable to assume *a priori* that the family of the λ_--characteristic curves of the simple wave R_{25} extend to the sonic curve RV and reflect off it as a family of λ_+-characteristic curves. Here the extension of R_{25} is not a simple wave because the solution must vary along both λ_- and λ_+ characteristics.

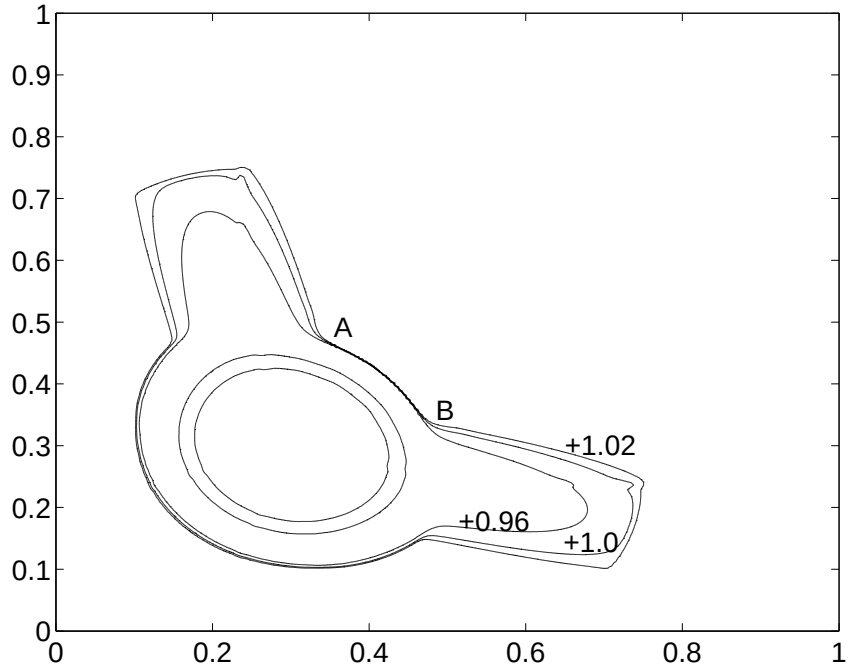

Figure 4.1.8: Comparison of wave filter shock location A, B and pseudo-Mach number contour plots at $\theta = 22.5^o$ with 800×800 mesh.

The solution is jointly determined by the subsonic domain and the supersonic domain. These reflected λ_+-characteristic curves reach a curved boundary WV, which forms another degenerate Goursat problem with the support of a straight λ_+-characteristic line $WX$and a curved λ_--characteristic line WV. This degenerate Goursat problem has a simple wave solution whose data are on the left boundary QP' since adjacent to the WX side is the constant state (ρ_5, u_5, v_5, p_5). The numerical results indicate that this reflected simple wave is a compressive wave and forms a shock with starting point V. See Fig. 4.2.2, where characteristic distance denotes the 'shock distance', i.e. the length of the reflected characteristics, and separation distance is the normal

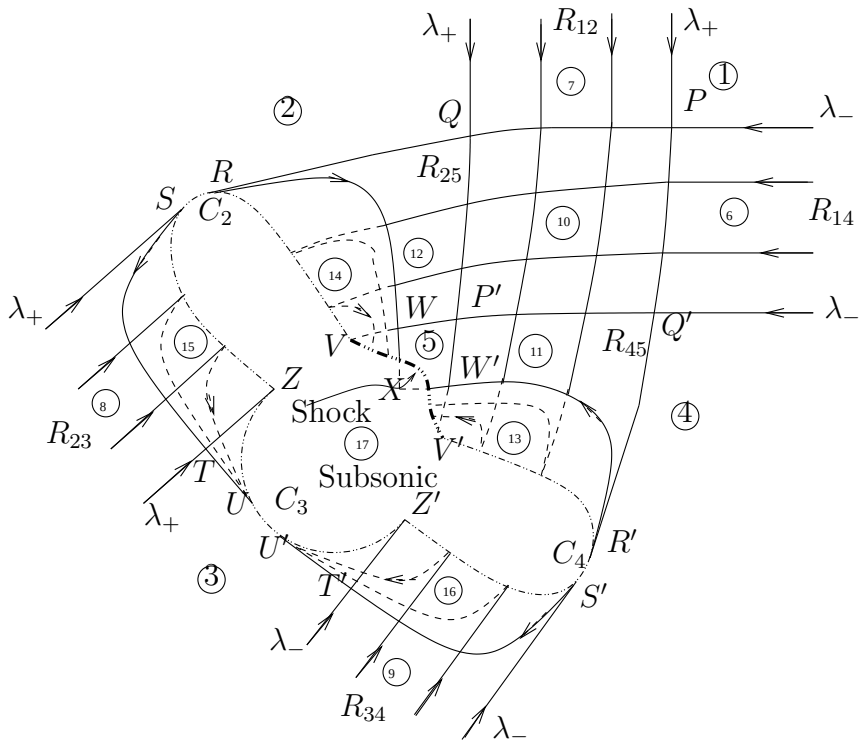

Figure 4.2.1: Generalized characteristic analysis for the case of four forward rarefactions in a 2D Riemann problem. Courtesy of J. Li and T. Zhang in [14].

separation between two neighboring characteristics. This plot shows the occurrence of the shock. The shock borders the constant domain (ρ_5, u_5, v_5, p_5). By symmetry, this structure is repeated across the symmetric axis with starting point V' of another shock in the primed variables $W'V'X$. The location of the sonic curve RV and the characteristics in the domain RVW are tangled together without a causal order and determined by the pseudo-transonic flow. Thus our interpretation of the reflection of the λ_--characteristic curves on the sonic curve RV is for illustration purposes only in the schematic Fig. 4.2.1.

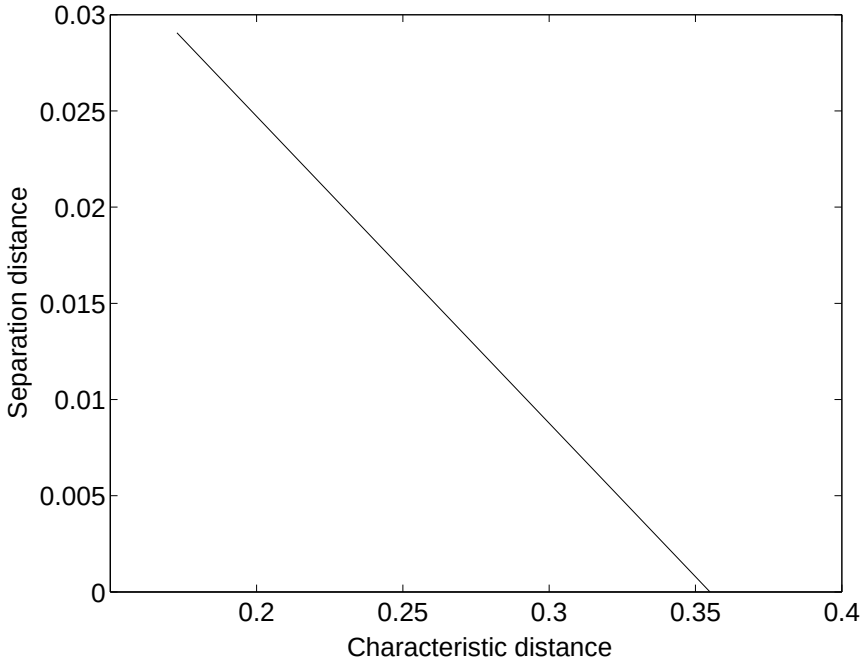

Figure 4.2.2: Plot of separation distance between neighboring characteristics starting on the sonic curve vs. distance along characteristics with $\theta = 22.5^o$.

We analyze the numerical results in Fig. 4.2.3 and Fig. 4.2.4, which show the variation of density ρ along pseudo-stream curves I and II, presenting regions corresponding to expansion and compression waves. The arrows on the stream curves indicate the direction of particle motion. In Fig. 4.2.4, the distance s denotes the distance along pseudo-stream curves I and II. The structure of the solution for the reflected characteristic curves R_{23} and R_{34} on the opposite side of the $x = y$ symmetry arc in Fig. 4.2.1 is clarified, where the family of λ_+-characteristic curves coming from R_{23} collide with a Tricomi type pseudo sonic curve SZ and are reflected to form a weak shock wave ZU, which resembles the 90^o case. A similar pattern appears on

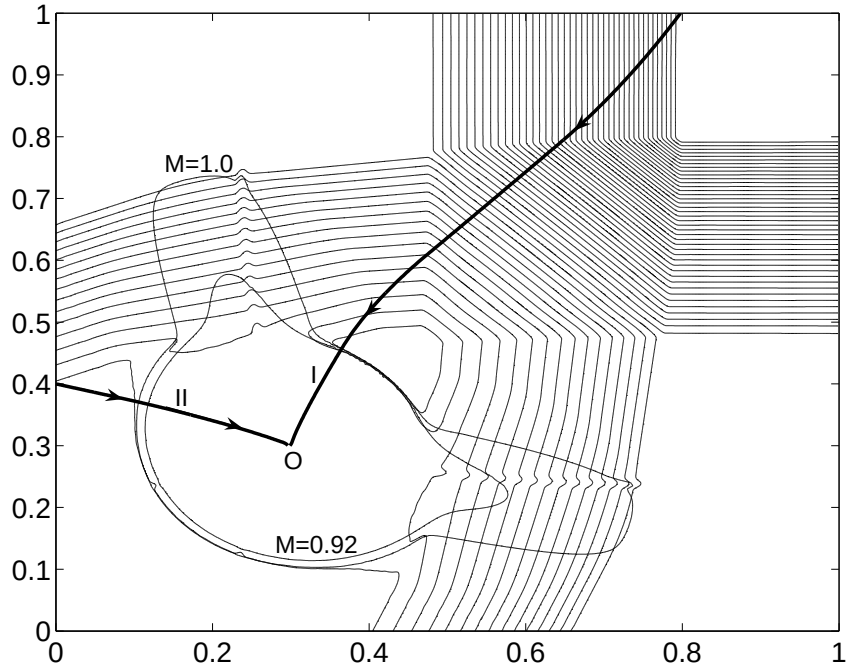

Figure 4.2.3: Density contours (light), two Mach contours (light) with $M = 1$, $M = 0.92$ and two pseudo-stream curves I, II (bold) which cut through the weak shock waves and shock waves in the neighborhood of the $M = 1$ contour shown at $\theta = 22.5^o$. The arrows on the stream curves indicate the direction of particle motion.

the other side. Characteristic curves from R_{45} reflect at the sonic curve $S'Z'$ to form another weak shock wave $Z'U'$. The two weak shock waves from the reflection of R_{23} and R_{34} end at U and U' respectively, which match numerical results in Fig. 2.6.2 and Fig. 2.6.3.

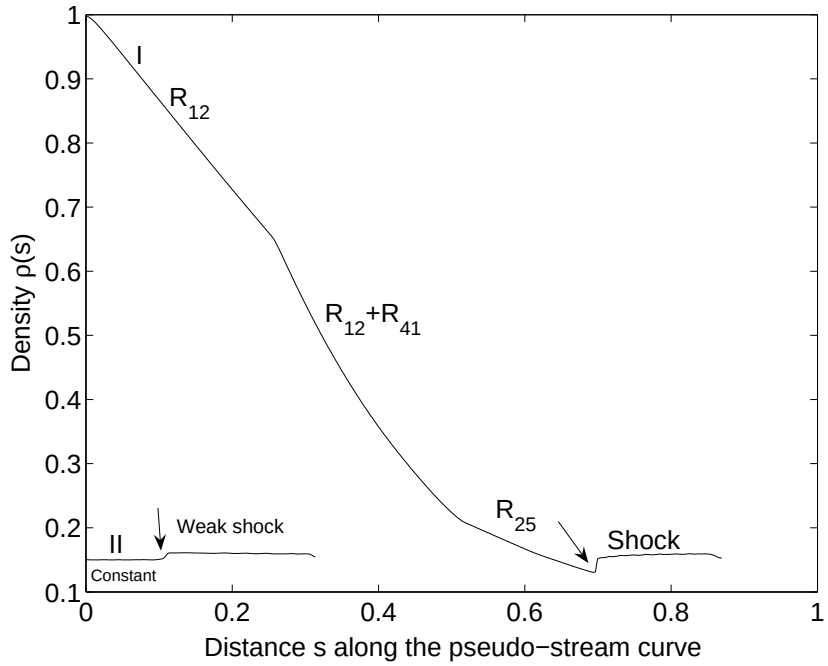

Figure 4.2.4: The increasing positions of (weak shock wave and shock wave) in the plot of $\rho(s)$ vs s plots are visible as bumps along two pseudo-stream curves I (above) and II (below) in Fig. 4.2.3.

4.3 Shock formation for two backward and two forward rarefaction waves

For the case of two backward and two forward rarefaction waves, there are two symmetric transonic shocks in the solution as shown in [2, 20, 22, 28] and see Fig. 4.3.1. The mechanism of shock formation is the same as was discussed for the case of four forward rarefaction waves in Fig. 4.2.1 because the part of Fig. 4.3.1 upper-right to $\xi + \eta = u_2 + v_2$ has the same structure as that of the corresponding part in Fig. 4.2.1.

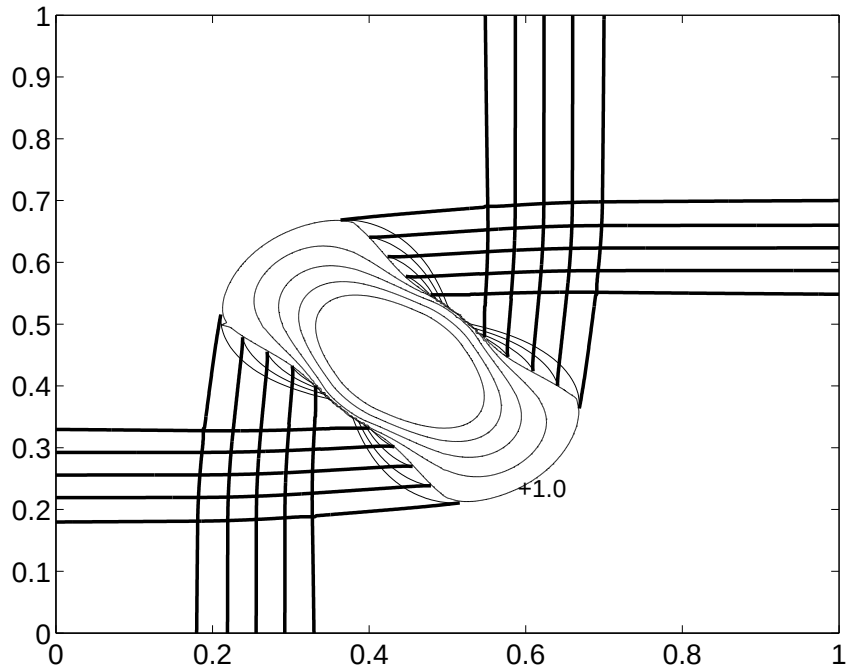

Figure 4.3.1: The case of two forward and two backward rarefactions oriented at 90^o with $p_1 = 0.444, \rho_1 = 1.0$, $u_1 = v_1 = 0.00$, $\rho_2 = 0.5197$, $T = 0.25$; characteristics (bold) and contour curves of pseudo-Mach number (light) are plotted.

Chapter 5

Conclusions

We discussed numerical simulations showing two distinct mechanisms for shock formation and supporting theoretical conjectures based on generalized characteristic analysis regarding mathematical mechanism in the 90^o case and the oblique rarefaction case. We also discovered that the same mathematical mechanism as in the oblique rarefaction case occurs for the shock formation for two forward and two backward rarefaction waves.

For the 90^o case, the interaction of two rarefaction waves of the same family and parallel at infinity leads to a pressure drop larger than that due to enter taken singly. Thus the interaction seems to 'over rarefy', leading to low pressure states incompatible with pressures given at infinity due to the same rarefactions considered individually. A shock wave results from the joining of these high and lower pressure regions. It is the interaction of rarefaction R_{41} and R_{23} and R_{34} and R_{12}, including the interaction of R_{41} and characteristics from constant state 3 below R_{23}, which produce this result. The shock formation for the oblique case has a possible physical mechanism similar to one found in stationary flow, which is illustrated schematically

in [14], see in Fig. 24, p. 741 there, associated with the numerical result in Fig. 2.6.3. Basically, a rarefaction reflection reflects at a sonic boundary; the reflected wave is a compression, which may in time break and become a shock. For the steady transonic small disturbance equation, shock reflection on a sonic curve is illustrated in Cole and Cook [9], see the shock formation over an airfoil in p. 314, Fig. 5.4.13. The structure of shock formation from the reflection of rarefaction waves on a sonic curve was suggested by Guderly [17], for the two-dimensional steady irrotation isentropic flow, they put forward a concept of shock formation from reflection of characteristics on a sonic curve. When a supersonic bubble appears on the top of an airfoil in an ambient subsonic domain, a family of characteristics are generated in the bubble from the surface of the airfoil, and they hit the rear portion of the sonic curve, and are reflected downstream to form a compressive wave which then forms a shock wave within the bubble. The subsonic region plays the role of a permeable obstacle which declines streamlines towards the airfoil and causes compressive waves. This is similar to the effect of a concave wall in the classical problem of supersonic flow over a smooth rigid wall. We point out the bump on the wall of the flow channel causes the shock formation naturally in Cole and Cook [9], where it has an important application in the study of a flow over an airplane wing. Furthermore, this formation of shocks seems to be the fundamental mechanism for the Guderly reflection pattern in Hunter and Tesdall [29].

For waves interacting with a sufficiently large oblique angle in the third quadrant, the sonic curve has an exaggerated non convex shape (rabbit ears). The curve extends into the rarefaction waves and interacts with them. The rarefactions are reflected

as compression waves along these rabbit ears, in the sense that along this part of the sonic curve, there are impinging λ_+ and λ_- characteristics. The characteristics coming from infinity are part of the rarefaction wave, while the reflected ones, as stated, are compressions. On the side facing the first quadrant, these compressions have sufficient travel distance to break and form a shock wave, centered at the 45^o line, where it crosses the $M = 1$ contour. On the side facing the third quadrant, due to the angle between the waves at infinity, there is a very weak shock on this side of the $M = 1$ contour, which can be analogously interpreted in Fig. 11 in [8, page 390], as stationary flow in nozzles and jets. Very likely these characteristics would have an envelope if they were not intercepted by a shock front. To prevent the envelope singularity, an "intercepting" shock is therefore necessary. The reason for the reflected wave to be a compression is illustrated by similarity to a related problem in aerodynamics, as discussed in the literature, and explained in [9] and [17].

The Riemann problem is typically unstable in that it is a locus of bifurcation for the Riemann data. Even in 1D, the isolated jump discontinuity holds only at time zero and (for gas dynamics) the solution at all positive times has three traveling waves.

However, it is stable in the sense of preservation of structure upon variation of initial (Riemann) conditions. In this sense, our analysis deals with representative variation of the initial conditions, but does not explore the complete seven dimensional space of nearby initial conditions numerically. This numerical stability analysis was conducted for the full Euler equations (2.1.1) rather than for the self-similar equations (2.1.2). No non-self-similar solutions were observed in the variations of the initial

data. We have studied systematically a variation of the angle between two of the four initial rarefaction waves. As this angle is modified sufficiently, we find a jump to a new solution branch, with a distinct mechanism (in a detailed sense) for the shock formation. Stability refers to a small variation of these waves in their strength or their angle. It is also stable under (a small) variation of the strength of the four waves. We expect that a large variation of the strength may cause a change in the details of the shock formation mechanism.

Although it is conceptually possible to allow an arbitrary number of waves, at arbitrary angles in the 2D Riemann problem formulation, the case of four waves is the case most commonly considered.

Bibliography

[1] M.-J. Bae, G.-Q. Chen, and M. Feldman, *Regularity of solutions to regular shock reflection for potential flow*, Inventiones Mathematicae, 2009 (to appear); DOI 10.1007/s00222-008–0156-4 (online); Preprint arXiv:0804.2500, April 2008.

[2] T. Chang, G. Chen, S. Yang, *On the 2-D Riemann problem for the compressible Euler equations, I. Interaction of shocks and rarefaction waves*, Discrete and Continuous Dynamical Systems, 1 (1995), pp. 555–584; *II. Interaction of contact discontinuities*, Discrete and Continuous Dynamical Systems, 6 (2000), pp. 419–430.

[3] G.-Q. Chen and M. Feldman, *Potential theory for shock reflection by a large-angle wedge*, Proc. National Acad. Sci. USA (PNAS), 102 (2005), pp.15368-15372.

[4] G.-Q. Chen and M. Feldman, *Global solutions to shock reflection by large-angle wedges*, Ann. Math. 2008, 106 pages (to appear; accepted on October 3, 2006).

[5] G.-Q. Chen and M. Feldman, Regular shock reflection-diffraction and von Neumann sonic conjecture, in preparation, 2008.

[6] S.-X. Chen, *Stability of a Mach configuration*, Comm. Pure Appl. Math. 59 (2006), pp.1-35.

[7] S.-X. Chen, *Mach configuration in pseudo-stationary compressible flow*, J. Amer. Math. Soc. 21 (2008), pp.63-100.

[8] R. Courant, K. O. Friedrichs, *Supersonic flow and shock waves*, Springer-Verlag, New York Inc., 1948.

[9] J. D. Cole, L. P. Cook, *Transonic Aerodynamics*, North-Holland, Amsterdam, 1986.

[10] P. Colella, *A direct Eulerian MUSCL scheme for gas dynamics*, SIAM J. Sci. Stat. Comput., 6 (1985), pp. 104–117.

[11] I M. Gelfand, *Some problems in the theory of quasilinear equations*, Usp Math Nauk, 14 (1959), pp.87-158; Amer. Math. Soc. Transl., 29 (1963), pp.295–381.

[12] J.Glimm, *Solutions in the large for nonlinear hyperbolic systems of equations*, Comm. Pure Appl. Math, 18 (1965), pp. 697-715.

[13] J. Glimm, J. W. Grove, Y. Kang, T. Lee, X. Li, D. Sharp, Y. Yu, K. Ye, M. Zhao, *Statistical Riemann Problems and a Composition Law for Errors in Numerical Solutions of Shock Physics Problems*, SIAM J. Sci. Comp., 26 (2005), pp. 666–697.

[14] J. Glimm, X. Ji, J. Li, X. Li, P. Zhang, T. Zhang, Y. Zheng,*Transonic shock formation in a rarefaction Riemann problem for the 2D compressible Euler equations*, SIAM J. Appl. Math., 69 (2008), pp.720-742.

[15] J. Glimm, H. C. Kranzer, D. Tan, F. M. Tangerman, *Wave Fronts for Hamilton-Jacobi Equations: The General Theory for Riemann Solutions in R^n*, Commun. Math. Phys., 187 (1997), pp. 647–677.

[16] J. Glimm, D. Sharp, *An S-matrix Theory for Classical Nonlinear Physics*, Foundations of Physics, 16 (1986), pp. 125–141.

[17] K. G. Guderly, *The theory of transonic flow*, Pergamon Press, London, 1962.

[18] A. Kurganov, E. Tadmor, *Solution of two-dimensional Riemann problems for gas dynamics without Riemann problem solvers*, Numerical Methods for Partial Differential Equations, 18 (2002), pp. 548–608.

[19] P. D. Lax, Hyperbolic system of conservation laws II. Comm. Pure Appl. Math, 10 (1957), pp. 537-566.

[20] P. D. Lax, X. Liu, *Solution of two-dimensional Riemann problems of gas dynamics by positive schemes*, SIAM J. Sci. Comp., 19 (1998), pp. 319–340.

[21] J. Li, *On the two-dimensional gas expansion for the compressible Euler equations*, SIAM J. Appl. Math., 62 (2002), pp. 831–852.

[22] J. Li, T. Zhang, S. Yang, *The Two-Dimensional Riemann Problem in Gas Dynamics*, Pitman Monographs 98, Longman, 1998.

[23] J. Li, T. Zhang, Y. Zheng, *Simple waves and a characteristic decomposition of the two dimensional compressible Euler equations*, Commun. Math. Phys, 267 (2006), pp. 1–12.

[24] J. Li, Y. Zheng, *Interaction of rarefaction waves of the two-dimensional self-similar Euler equations*, Arch. Rat. Mech. Anal., in press.

[25] X. Liu, P. D. Lax, *Positive schemes for solving multi-dimensional hyperbolic systems of conservation laws*,J.Comp. Fluid Dynam., 5 (1996), pp. 133–156.

[26] E. Mach, *Uber den verlauf von funkenwellenin der ebene und im raume*, Sitzungsber. Akad. Wiss. Wien, 78 (1878), pp.819-838.

[27] B. Riemann, *Uber die forpflanzung ebener luftwellen von endlicher schwingungsweitei*, Abhandl Koenig Gesell Wiss, Goettingen, 8 (1860), p43.

[28] C. W. Schulz-Rinne, J. P. Collins, H. M. Glaz, *Numerical solution of the Riemann problem for two-dimensional gas dynamics*, SIAM J. Sci. Comp., 4 (1993), pp. 1394–1414.

[29] A. M. Tesdall, J. K. Hunter, *Self-similar solutions for weak shock reflection*, SIAM J. Appl. Math., 63 (2002), pp. 42–61.

[30] Y. Yu, M. Zhao, T. Lee, N. Pestieau, W. Bo, J. Glimm, J. W. Grove, *Uncertainty Quantification for Chaotic Computational Fluid Dynamics*, J. Comp. Phys., 217 (2006), pp. 200–216.

[31] T. Zhang, Y. Zheng, *Conjecture on the structure of solutions of the Riemann problem for two-dimensional gas dynamics systems*, SIAM J. Math. Anal., 21 (1990), pp. 593–630.

[32] Y. Zheng, *Systems of Conservation Laws: Two-Dimensional Riemann Problems*. Series: Progress in Nonlinear Differential Equations and Their Applications, 38, Birkhäuser, Boston, Cambridge, MA, 2001.